

pubs.acs.org/journal/abseba Article

# Increase in Charge and Density Improves the Strength and Toughness of Mussel Foot Protein 5 Inspired Protein Materials

Jacob J. Graham and Sinan Keten\*



**Cite This:** ACS Biomater. Sci. Eng. 2023, 9, 4662–4672



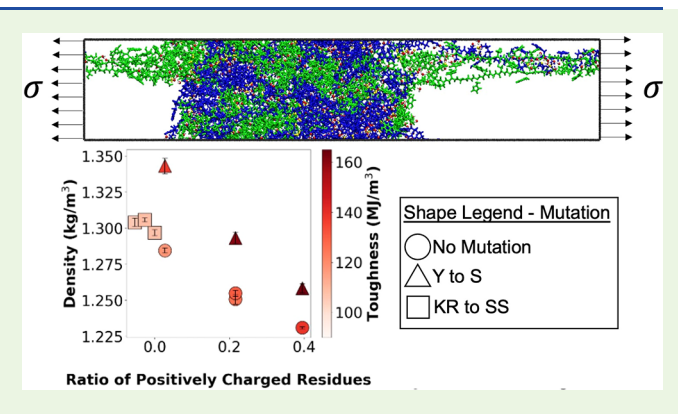
**ACCESS** 

Metrics & More

Article Recommendations

Supporting Information

ABSTRACT: Mussel foot protein 5 (fp5) found in the adhesive byssal plaque of Mediterranean mussel *Mytilus galloprovincialis* exhibits exceptional underwater adhesion to diverse surfaces to the extent that adhesion strength typically exceeds the cohesive strength of the plaque. While sequence effects such as presence of charged residues, metal ion coordination, and high catechol content have been identified to govern fp5's interaction with surfaces, molecular contributors to its cohesive strength remain to be fully understood. Addressing this issue is critical for designing mussel-inspired sequences for new adhesives and biomaterials enabled by synthetic biology. Here we carry out all-atom molecular dynamics simulations on hydrated model fp5 biopolymer melts to understand how sequence features such as tyrosine and charge



content affect packing density and inter-residue and ionic interaction strengths and consequently influence the cohesive strength and toughness. Systematic serine (S) substitutions for lysine (K), arginine (R) and tyrosine (Y) residues reveal that Y to S substitution surprisingly results in improvement of cohesive strength due to densification of the material by removal of steric hindrances, whereas the removal of charge in K and R to S substitutions has a detrimental impact on strength and toughness as it reduces cohesive interactions facilitated by electrostatic interactions. Additionally, melts formed from split fp5 sequences with only C or N terminal halves show distinct mechanical responses that further illustrate the role of charge. Our findings provide new insights for designing materials that could potentially surpass the performance of existing biomolecular and bioinspired adhesives, specifically by tailoring sequences for balancing charge and excluded volume effects.

**KEYWORDS:** mussel foot protein, molecular dynamics,  $\pi$ -cation, adhesives, charge, cohesion

#### 1. INTRODUCTION

People have long been fascinated by marine mussels for their abundance, tenacity, and nutritional value. Their ability to stably affix themselves to various underwater surfaces including each other's shells makes them a focal point for scientists and gourmets alike. In the span of just a few minutes, these remarkable organisms are able to synthesize strong threads terminating in sticky pads capable of astonishing underwater adhesion. 1-3 Formation of these threads continues repetitively until an array stretches out radially protecting the mussel in turbulent conditions.4 The plaque's firm wet adhesion has prompted rapid progress in identifying and characterizing constituents of the byssal threads across species.<sup>5-7</sup> So far, these efforts have helped to identify six unique proteins localized in the plaque, 8-12 with evidence of ten more 10,13 confirmed to exist in the threads' collagenous core, 7,14 and proven the existence of recoverable catechol-Fe complexes in the outer cuticle. 15-19 Mussel foot proteins have become famous for their distinctively high L-3,4-dihydroxyphenylalanine (DOPA) content, which is hypothesized to play pivotal roles in both adhesion and cohesion. Although DOPA has significant presence in the

cuticle, in the core, and throughout the plaque, it is particularly prevalent in fp3 and fp5, proteins that are localized to the adhesive interface. DOPA, which is a post-translational modification of Y, possesses a unique ability to interact with polar surfaces and solvents, cross-link with itself, participate in  $\pi$ -cation bonding, and form metal-coordination complexes by reducing to DOPA semiquinone. While the DOPA modification improves underwater adhesion and the strength of the metal-coordination complexes, it is not a necessary modification for strong cross-linking and it reduces the strength of  $\pi$ -cation interactions which rely primarily on the aromatic component of tyrosine. If p3 and fp5 have inspired biomimetic adhesives for surgical applications, synthetic adhesives like poly(catecholstyrene), and even fp5 and silk hybrid materials 28,29

Received: January 19, 2023 Accepted: June 13, 2023 Published: July 7, 2023

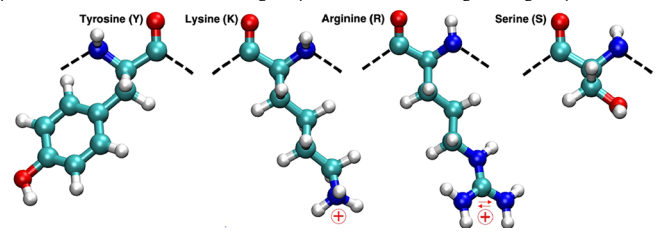




Table 1. Naming Convention for All of the fp5 Systems Studied, Average Net Charge per Chain, and Sequences of Each Chain Type<sup>a</sup>

naming convention	average net charge per chain (+)	sequences
Cfp5	15	Nfp5: SSEEYKGGYYPGNTYHYHSGGYYHGSGYHGGYKGYYG; Cfp5: KAKKYYYKYKNSGKYKYLKKARKYHRK GYKKYYGGGSS
Nfp5-Cfp5	8	
Nfp5	1	
Cfp5(YtoS)	15	$\label{eq:mfp5} Nfp5(YtoS): SSEESKGGSSPGNTSHSHSGGSSHGSGSHGGSKGKSSG; Cfp5(YtoS): KAKKSSSKSKNSGKSKSLKKARKSHRKGSKKSSGGGSS$
Nfp5- Cfp5(YtoS)	8	
Nfp5(YtoS)	1	
Cfp5(KRtoSS)	0	Nfp5(KRtoSS): SSEEYSGGYYPGNTYHYHSGGSYHGSGYHGGYSGSYYG; Cfp5(KRtoSS): SASSYYYSYSNSGSY SYSYLSSASSYHSSGYSSYYGGGSS
Nfp5- Cfp5(KRtoSS)	-1	
Nfp5(KRtoSS)	-2	
fp5	16 <sup>b</sup>	fp\$ full sequence: SSEEYKGGYYPGNTYHYHSGGSYHGSGYHGGYKGKYYGKAKKYYYKYKNSGKYKYLKKARKYH RKGYKKYYGGGSS

<sup>a</sup>The Nfp5 chains have a net charge of +1, while the Cfp5 chains have a much greater net charge of +15. Bold letter S represents the point mutations. <sup>b</sup>In the fp5 system, there are only 12 chains instead of 24 since fp5 is the equivalent of the Nfp5 and Cfp5 bonded sequentially. Therefore, the average charge density is the same between the fp5 system and the Nfp5–Cfp5 system.



revolutionizing the field of wet adhesives. Still, the debate over exact mechanisms of byssal adhesion is controversial with circulating theories of surface covalent bonding, cooperation between adjacent K and Y residues at the interface,  $^{30,31}$  Coulomb attraction, and hydrogen bonding. No single mechanism has been identified that can fully describe this phenomenon. Similarly, there are many arguments surrounding cohesion, which often dictates yield and failure of the byssus. There is strong evidence suggesting that disulfide bonds,  $^2$  DOPA cross-links,  $^{33}$  metal-coordination complexes,  $^{15}$  and  $\pi$ -cation bonds between aromatics and basic amino acids contribute to cohesion.  $^{21}$  It remains challenging to study these factors with molecular resolution.

Data-driven techniques such as machine learning assisted directed evolution, 34-37 data centralization, 38 and multiscale modeling<sup>39,40</sup> have emerged as the leading strategies for predicting mechanical properties of synthetic biomaterials from sequence. Here we used a molecular dynamics (MD) approach, 4,41 which offers exact control over sequences and mutations, to investigate the impact of the aromatic component of tyrosine (Y) and basic amino acids lysine (K) and arginine (R) on the mechanical properties of mussel foot protein 5 of the Mediterranean mussel Mytilus galloprovincialis. Together, Y and positively charged amino acids make up 26 and 21 mol % of the protein, respectively, and are often found in neighboring pairs. While Y is evenly distributed across the 76-residue sequence, with ten residues in the first half and ten residues in the second half, K and R are mostly concentrated to one half of the protein. Our original hypothesis was that mutation of Y to serine (S) would diminish cohesion by removing the possibility of  $\pi$ stacking and  $\pi$ -cation bonding. This result was previously shown experimentally by Gebbie et al. using an underwater surface force apparatus and fp mimetic peptides.<sup>21</sup> To test this same idea using a similar all-atom MD approach, we split the

protein into two halves, with each having identical Y content but variable amounts of charged residues. From now on, the chain made up of the 38 residues closest to the N-terminus in fp5 will be referred to by the abbreviation Nfp5, and the chain made up of the 38 residues closest to the C-terminus will be referred to with the abbreviation Cfp5. By simulating mixtures of the resulting chains, we sought to show that systems rich in both Y and charged residues exhibited the best cohesion. Instead, by systematically mutating Y, K, and R to S, we discovered an outsize role of net charge and density on toughness and maximum stress but failed to correlate interactions between Y and basic residues to cohesion. Our work demonstrates how sequences can be tailored to balance charge and excluded volume effects to aid the discovery of new biomaterials with enhanced properties.

#### 2. RESULTS AND DISCUSSION

Table 1 lists the composition of the ten simulations that were performed to observe how Nfp5 and Cfp5 chains interacted with one another and how the presence of Y and basic residues impacted mechanical properties. The first three rows of Table 1 describe a homogeneous melt of Cfp5 chains, a mixture of the two chain types in equal molar fraction named Nfp5-Cfp5, and a homogeneous melt of Nfp5 chains. The full amino acid sequences for the Nfp5 and Cfp5 chains coming from fp5 are provided in the third column. In total, each one of these simulations contains 24 protein chains, 10% water content by mass, and just enough ions to neutralize the net charge of the system. The disproportionate amount of K in Cfp5 makes the net charge per chain drastically larger than that of Nfp5, which is reflected in column 2 of Table 1. The same simulations were repeated with all Y mutated to S (YtoS) and then again with all the charged K and R mutated to S (KRtoSS). Serine was chosen as the substitute residue because it lacks the aromatic

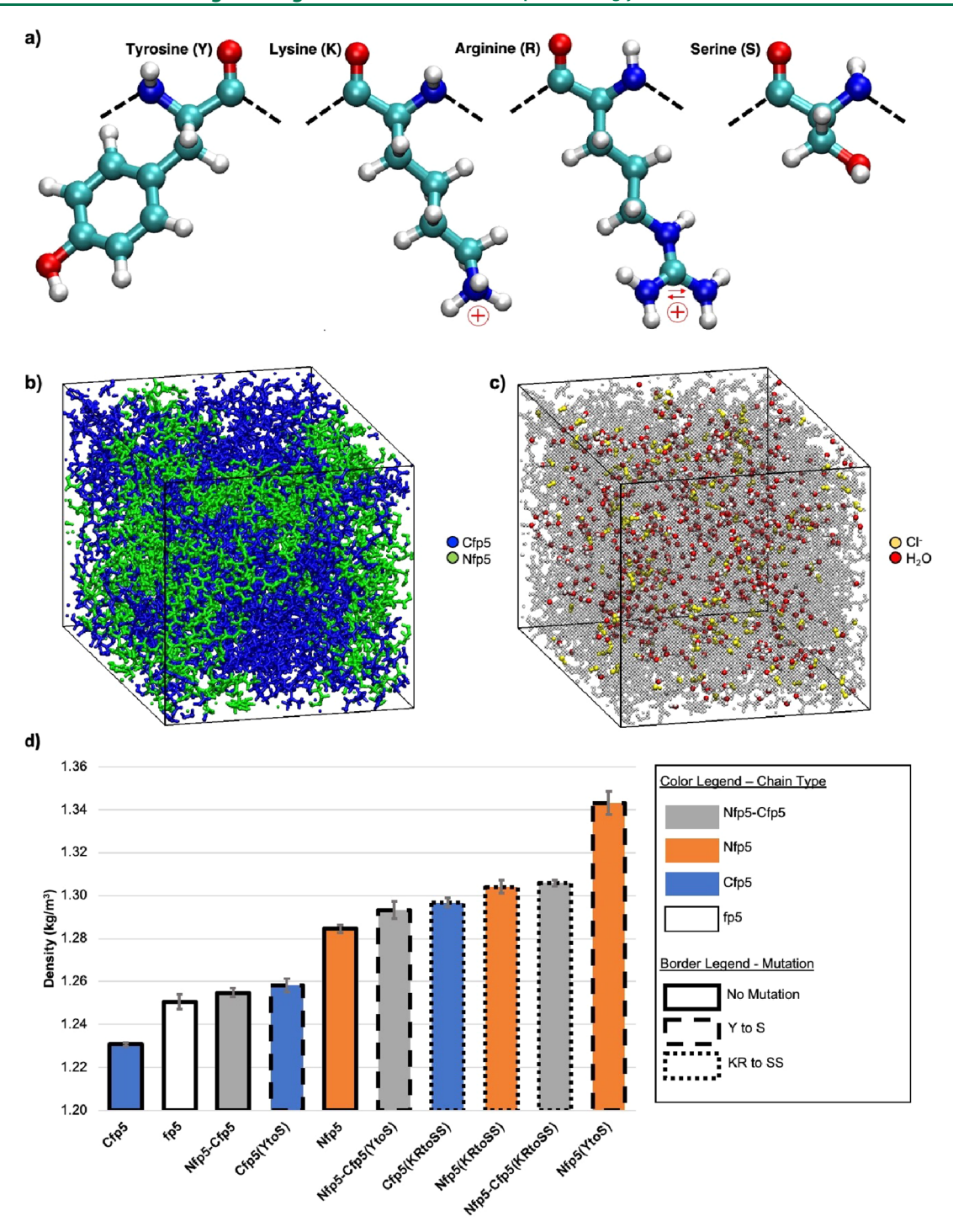


**Figure 1.** Equilibrium state of fp5 disordered melt systems and variants. (a) Visual representations of Y, K, R, and S. Since K and R are modeled in their protonated states, atoms modeled as carrying a net charge are labeled to reflect that. Arrows on the R diagram represent that the residue is stabilized by resonance, and charge is shared equally between two amines. Atom colors are assigned by the following key: nitrogen, blue; carbon, turquoise; hydrogen, white; oxygen, red. (b) Graphical representation of the Nfp5—Cfp5 system as an example with Cfp5 chains in blue and Nfp5 chains in green without visualizing water and ions. (c) Graphical representation of the same system portraying Nfp5 and Cfp5 as gray and translucent to highlight the dispersion of chloride and water. (d) Equilibrium density of each system averaged over 1 ns at 1 atm and 300 K plotted with error bars representing the standard deviation across five independent MD runs.

component of Y while preserving the hydroxyl group. Visualizations of each of these residues are depicted in Figure 1a with positively charged chemical groups of K and R labeled with a red plus symbol. Additionally, a tenth control simulation consisting of 12 full-length fp5 proteins with the same water and chloride content as the Nfp5—Cfp5 systems was meant to independently

capture the impact of chain splitting. All of the simulations were repeated five times with different initial configurations.

Results for the equilibrium density of each system type are reported in Figure 1d. See section 4.2.1 for description of density calculation. Panels b and c in Figure 1 show snapshots of the Nfp5—Cfp5 system upon reaching equilibrium, demonstrating

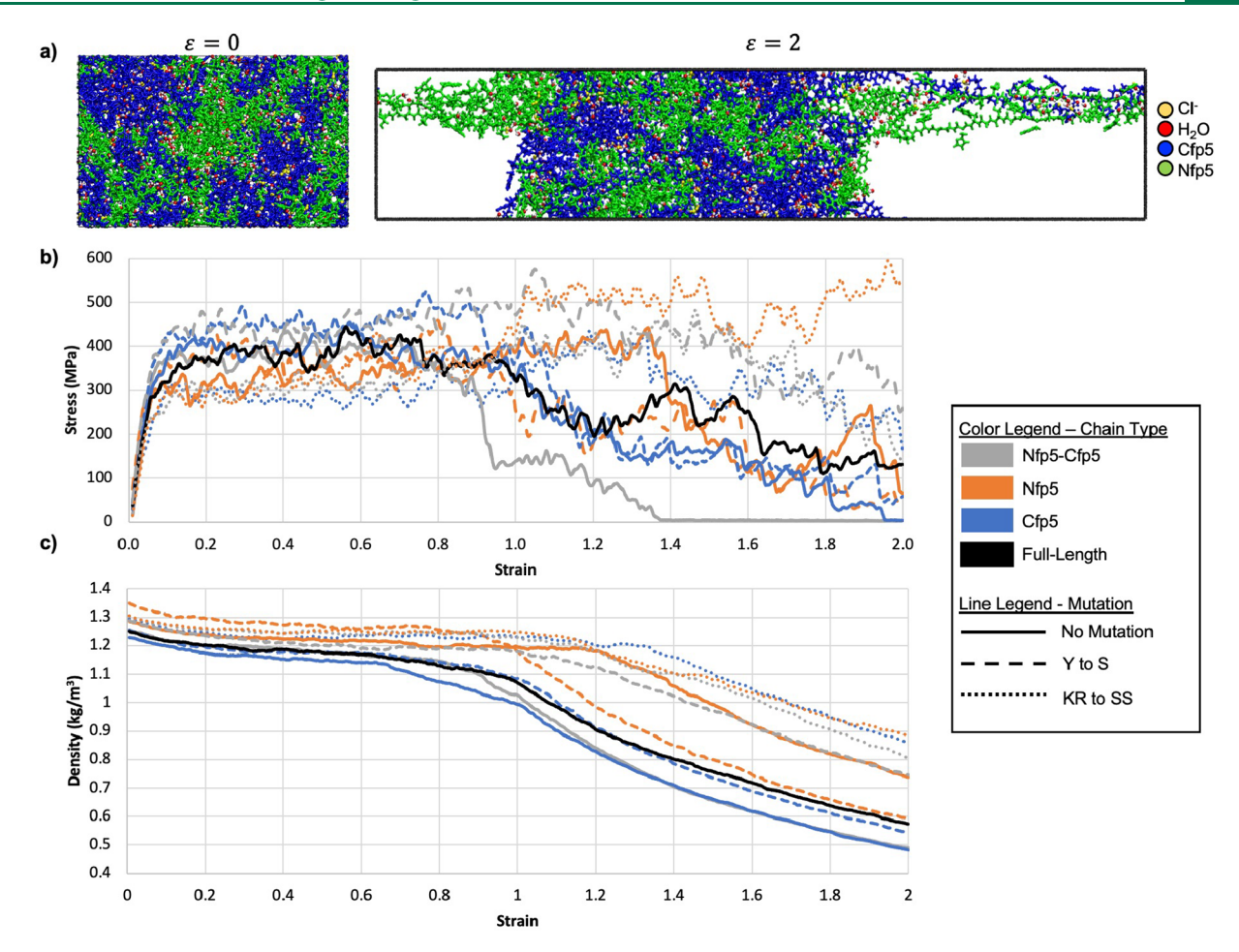


Figure 2. Bulk mechanical behavior during uniaxial tensile testing simulations. (a) Graphical representations of the Nfp5—Cfp5 system as an example with protein, water, and chloride color coded. (b) Stress plotted as a function of strain from 0 to 200% through one of the five MD runs. (c) Density plotted against strain from 0 to 200% over the same MD run as panel b.

that water and chloride are dispersed throughout the system. The Cfp5 system had the lowest density of 1.230 kg/m<sup>3</sup> due to the dramatic repulsive Coulomb potential between Cfp5 proteins, which carry a net positive charge on nearly 40% of residues. Plots in Figure S8 show the radial distribution functions of chloride around charged K, R, and glutamic acid (E) and neutral residues which confirm that chloride number density within 5 Å of basic residues is consistently higher than that around neutral and negatively charged residues (E). However, the repulsion was only partially mitigated by addition of the chloride counterions. The Nfp5 system had a notably higher density of 1.285 kg/m<sup>3</sup> since only 2.6% of residues in that system carry a net positive charge. In comparison, the Nfp5-Cfp5 system had an intermediate density of 1.255 kg/m<sup>3</sup>. Densification was observed for both mutations to varying degrees, depending on the types of protein present in the system. Mutating Y to S increased the density of Nfp5, Cfp5, and Nfp5-Cfp5 which is mostly attributed to a reduction in steric hindrance by Y's side chain. Nfp5 and Cfp5 have identical Y contents of 26%, but since Cfp5 packed more loosely, density increased by just 2.2% with the Y to S mutation compared to a 4.6% increase in the Nfp5 system. Tyrosine already readily occupied the space between Cfp5 proteins, which meant that steric hindrance had a smaller influence on chain spacing. The KR to SS mutation caused a drastic increase in density of 5.4% due to the diminished charge density. Densification of 1.5% for

the Nfp5(KRtoSS) system was less dramatic since there was a small proportion of K and R to begin with and is mostly due to S's smaller side chain. fp5 reached an average density just 0.3% below Nfp5—Cfp5 indicating that splitting fp5 in half had little impact on the equilibrium density.

In mixtures of two polymeric species, phase separation can occur if interactions between like chains are energetically favorable over those of unlike chains. When this happens, the material properties can vary dramatically with the size and shape of the separated phases. In the fp5 system, phase separation is limited since the two halves of the chains are bonded, although there may still be preferential alignment. Although it would be unusual for phase-separation to occur over this time scale, the number of like and unlike chain contacts were quantified for the Nfp5-Cfp5, Nfp5-Cfp5(YtoS), and Nfp5-Cfp5(KRtoSS) systems in Figure S4 to confirm that significant phase separation did not arise from splitting fp5. Each contact counted in Figure S4a represents an instance in which the center of mass of two residues fell within 7 Å of one another, excluding those neighboring residues that were directly bonded to one another. The number of contacts naturally increased with the two mutations of Y to S and KR to SS, but there was not a significant difference in the proportion of like versus unlike contacts. Based on the disproportionately high percentage of contacts between unlike chain species in Figure S4, the unlike contacts were slightly favored over like contacts meaning that the chains were

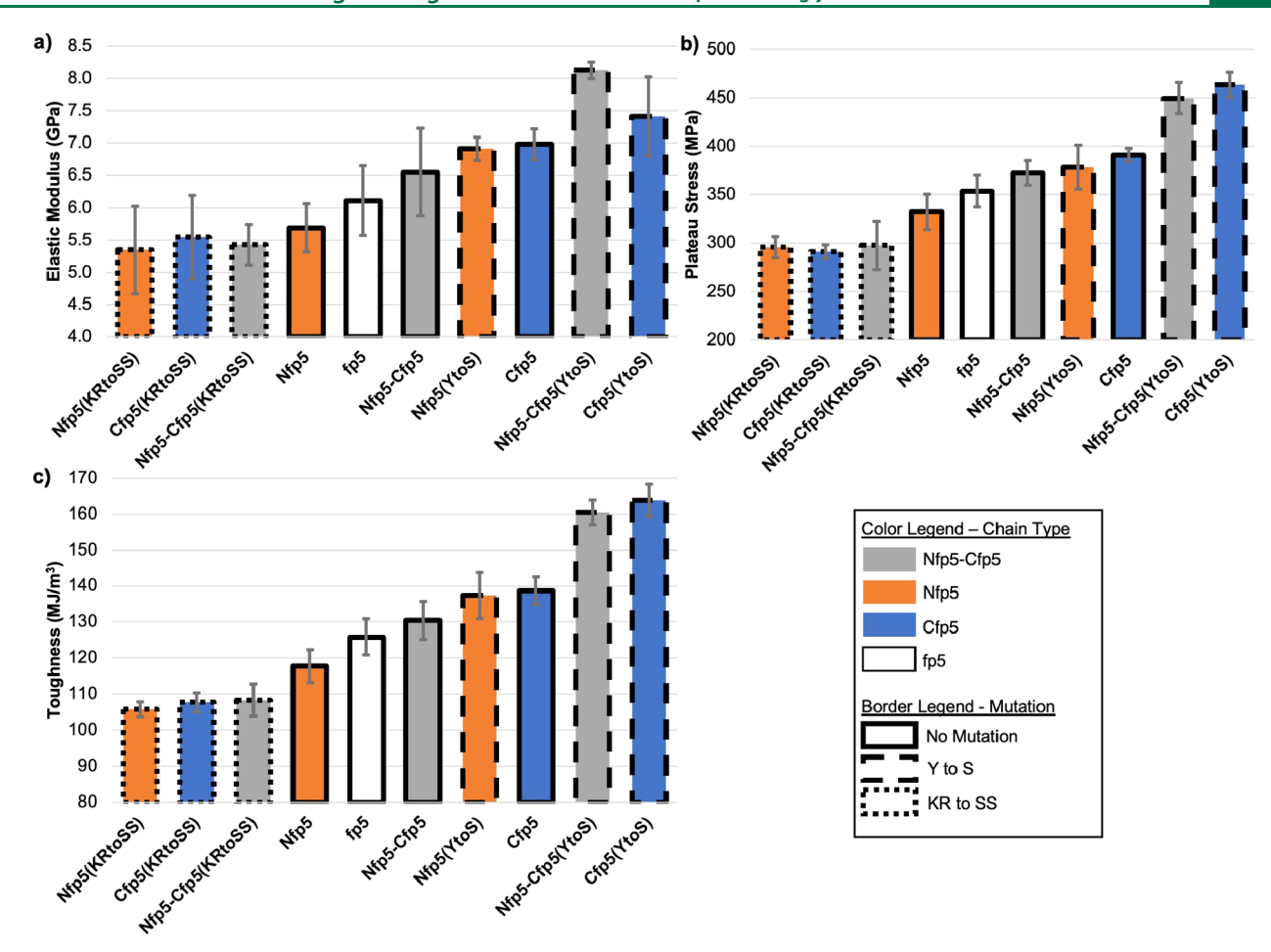


Figure 3. Characterization of all fp5 melt mechanical properties. (a) Elastic modulus (GPa) as defined by the slope between 0.01 and 0.03 strain. (b) Plateau stress (MPa) averaged between 0.20 and 0.40 strain. (c) Toughness averaged from 0 to 0.40 strain.

evenly mixed. Lack of phase separation was verified by the even mixture of chain types apparent in Figure 1b.

Next, we present results from the tensile simulations. The purpose of these analyses is to observe how mechanical properties change across chain types and with mutations. The stress—strain relation for the first run is shown in Figure 2b. Large fluctuations in stress are clearly visible, making it difficult to exactly determine the yield and breaking points. At strains beyond  $\epsilon \approx$  0.9, stress diverged as voids, which are evident in Figure 2a at  $\epsilon \approx 2$ , nucleated, and grew at variable rates. Void formation corresponded directly with steep drops in density, beginning around  $\epsilon \approx 0.90$  for the Nfp5–Cfp5 system and  $\epsilon \approx$ 0.66 for Cfp5 in Figure 2c which depicts the results of just one of the five repeat simulations. Consistently, the density sharply decreased simultaneously with stress in Figure 2b indicating that the onset of void formation is accompanied by partial mechanical failure. Sometimes multiple voids formed separately from one another, as in the Cfp5 system at  $\epsilon$  = 0.66 and  $\epsilon$  = 1.02. Mechanical failure, which depends heavily on void nucleation, could be pinpointed fairly accurately as knee points in the density curve. Since these knee points are defined by their downward concavity, the second derivative of the density with respect to strain was calculated, and local minima of the curvature were used to exactly quantify void onset. The strain at void onset was averaged over the five MD runs and reported with standard deviation in Figure S1. These values were highly inconsistent between MD runs but mostly fell between  $\epsilon \approx$ [0.90, 1.25]. The same mechanical tests were also performed on

melt systems with 30% and 50% water up to strain of 1. These tests, summarized in Figure S6, revealed that, while the material is weakened with increasing water content, density dependence on strain is reduced and no voids are identified up to strain of 1 for any system. This behavior has been observed with other protein materials and suggests that voids are stabilized by rearrangement of water molecules. Since the error in void onset was so high for each system, little can confidently be said regarding the relationship between mutations and the onset of mechanical failure. However, for each of the five runs, void formation was never observed below 0.40 strain. In fact, a plateau stress value was achieved on each system that stayed approximately unchanged between  $\epsilon = 0.20$  and 0.40. The plateau stress between these two values of strain was reported in Figure 3 and used as a parameter for the overall system strength.

The same strain cutoff of 0.4 was also used to quantify toughness as the integral of the stress data over the range of 0 to 0.40 strain. In Figure 3, the elastic modulus (MPa), plateau stress (MPa), and toughness (MJ/m³) were averaged and reported and are ranked on the x-axis in ascending order based on increasing average toughness (MJ/m³) values in Figure 3c. Based on this ranking, it was immediately obvious that the protein melts with the KR to SS mutation exhibited a lower overall toughness and plateau stress. Since all of the melts followed similar constitutive behavior, yielding before 0.10 strain and achieving a plateau stress that is held over 0.20 to 0.40 strain, toughness is mostly if not entirely dependent on the plateau stress achieved. The only difference in ranking toughness

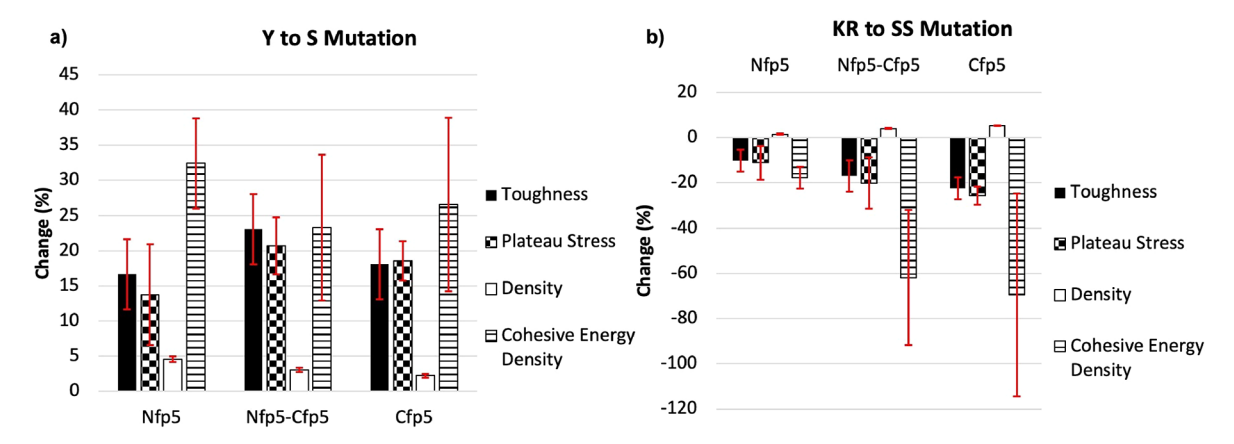


Figure 4. Impact of the (a) Y to S and (b) KR to SS mutations on toughness, plateau stress, density, and cohesive energy density for homogeneous and mixed chain type fp5 melts.

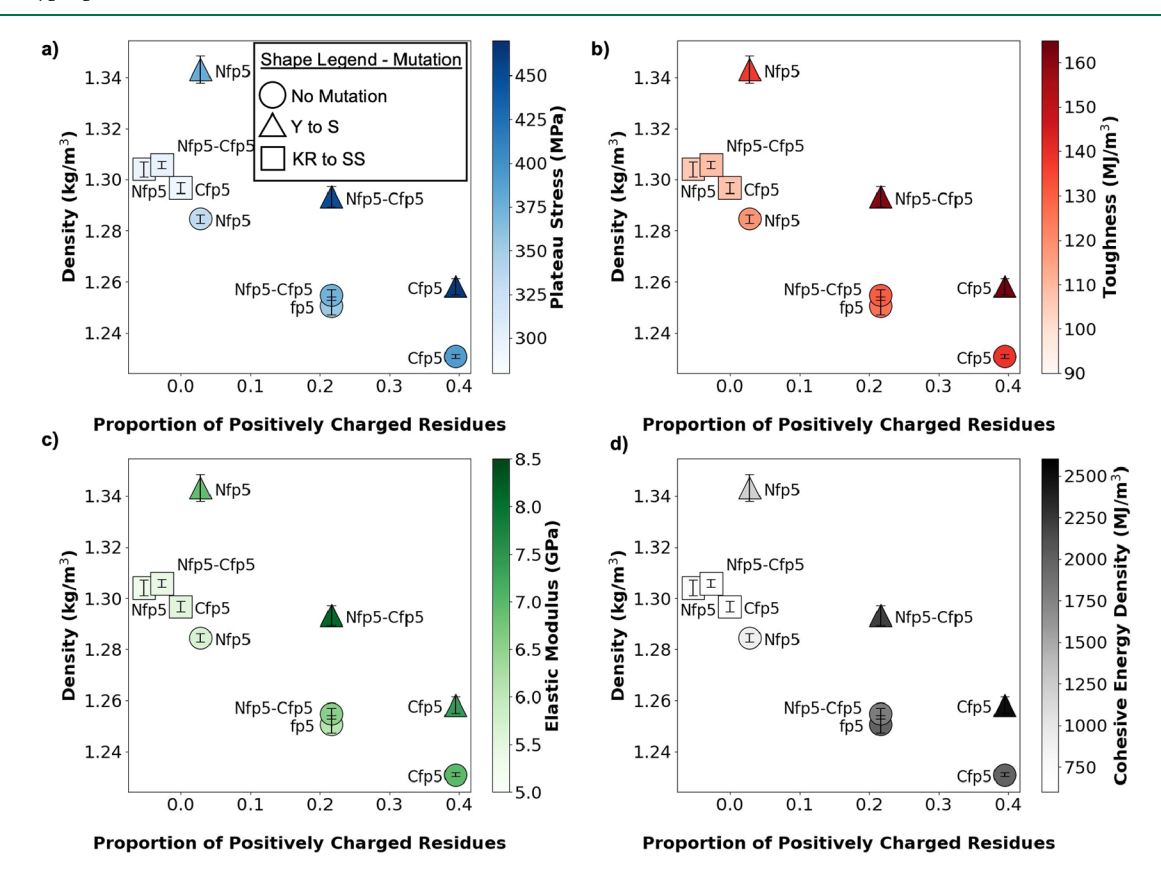


Figure 5. Density and proportion of positively charged residues are negatively correlated, while both variables positively correlate with mechanical properties (a) plateau stress (MPa), (b) toughness (MJ/ $m^3$ ), (c) elastic modulus (MPa), and (d) cohesive energy density (MJ/ $m^3$ ) that are represented by color gradient shading. Each data point is annotated with the type of chain in the system and mutation or lack thereof is specified by the marker shape indicated in the shape legend.

and plateau stress in panels b and c of Figure 3 is minor change in rank of those low strength systems with the KR to SS mutation, which all fall within a single standard deviation of one another anyway. For the simulations without mutations, the rank orders of toughness and plateau stress were the same, with Nfp5 being the weakest system, fp5 and Nfp5—Cfp5 having intermediate strength, and Cfp5 having the highest strength. Introducing the Y to S mutation substantially increased plateau stress and toughness in all cases. The percent increase is quantified in Figure 4a. Estimations of elastic modulus, defined as the slope between 0.01 and 0.03 strain provided inconclusive results for the impact of these mutations on Nfp5, but similar mutation-

dependent trends were observed for the Nfp5—Cfp5 mixture and Cfp5 where the KR to SS mutation decreased stiffness and the Y to S mutation increased stiffness.

To more clearly represent the impact of mutation on mechanical properties, the change in plateau stress and toughness as a result of the mutations was calculated and reported for the Y to S mutation in Figure 4a and for the KR to SS mutation in Figure 4b. The Y to S mutation increased toughness and plateau stress of NfpS and CfpS by 15% and 18%, respectively, while the mixture of NfpS and CfpS saw an even larger increase in both values. On the other hand, the KR to SS mutation decreased plateau stress and toughness in a manner

that scaled with the number of residues mutated. Since the Nfp5 systems without mutation had just a 2.6% fraction of positively charged residues, replacing those residues with S decreased toughness and plateau stress by approximately 10%. The Cfp5 systems carried positive charges on nearly 40% of the residues, so there was a larger decrease in toughness and plateau stress of 22.5% and 26%, respectively, with the replacement of charged residues with S. Following this trend, the drop in toughness and plateau stress of the Nfp5—Cfp5 simulations fell between that of the Nfp5 and Cfp5 melts. Although the S mutations increased the density of every system, the correlation with mechanical properties was opposite for the Y to S mutation versus the KR to SS mutation. Densification on its own is therefore insufficient to describe the effects of these mutations on properties.

Besides the aromatic component of Y, a critical difference between the two mutations is the impact on electrostatic interactions. Although both mutations caused an increase in density, mutating KR to SS reduced the net charge, while mutating Y to S only affected density. To represent the conflicting influence of density and net charge on mechanical properties and cohesive energy density, density was plotted against proportion of charged residues in Figure 5a—d with plateau stress, toughness, elastic modulus, and cohesive energy density color coded.

The symbolic labeling in Figure 5 demonstrates that the negative correlation between charge and density is conserved but shifted toward higher average density with the Y to S mutation. The color gradient of all three mechanical properties shows that properties increase with increasing density but also with increase in the number of charged residues on each chain which is why the CfpS(YtoS) system outperformed the others. This suggests that there are two critical components contributing to bulk cohesion. Replacing Y with S improves cohesive energy density by allowing tighter chain packing and shifting average contact positions toward the minimum of the effective potential well between residues. Conversely, the KR to SS mutation increases density to a similar degree but removes the powerful electrostatic interactions facilitated by chloride which enhances cohesive energy density of the bulk.

#### 3. CONCLUSION

Systematic mutation of basic and aromatic residues of fp5 in these MD simulations did not suggest that cation  $-\pi$  interactions between these residues played an important role in cohesion. The individual mutation of K, R, and Y, which are all but proven to contribute to cation- $\pi$  interactions, was expected to dramatically impact cohesive energy. Instead, for bulk protein melts of fp5 with 10% water composition by weight, the packing density of the protein, which is hindered by the presence of Y, and electrostatic interactions between charged amino acids and ions contribute more to strength and toughness. Powerful electrostatic potentials between K-rich positively charged Cfp5 chains and the surrounding chloride facilitate cohesion, where there would otherwise be chain repulsion. Unfortunately, this repulsion still results in an overall lower density, which forces the surrounding residues to interact at a suboptimal distance. This behavior is particularly prevalent in the low water-content systems considered in this study. Contrarily, in dense systems, steric hindrance from Y is magnified, which is reflected in the dramatic densification of all systems where Y is mutated to S. Based on the trend in Figure 5, these effects are at odds with low density, highly charged systems achieving similar strength and stiffness as that of high density and more neutrally charged

systems. Here, it is shown that at high strain rate and low water content, charge and density dominate the mechanical properties of adhesive protein fp5 of *Mytillus galloprovincialis*, but further investigation must balance other parameters such as water content, ion species, DOPA and phosphoserine content, and cross-linking density. On top of this, advantageous changes in primary sequence, like those introduced by nature's meandering evolutionary strategy, must be systematically identified to truly capture the relationship between sequence, property, and function. Ultimately, precise control of properties can be achieved, as is demonstrated by natural biomaterials, but discovery of new synthetic biomaterials will require scalable experimental and computational techniques for characterization and property prediction.

#### 4. METHODS

The initial structures of all proteins were generated with a random and extended conformation to reflect their intrinsically disordered nature. Initial dihedral angles were limited to a specific range to extend each chain and avoid particle overlap. Water was added to achieve a mass ratio of 10% with only enough ions to neutralize the net charge on each chain. Both equilibrium MD and tensile tests were conducted using Large-scale Atomic/Molecular Massively Parallel Simulator (LAMMPS). 43 First, each system underwent pressure and temperature annealing in an NPT ensemble to achieve an equilibrium state and rapidly sample a wide conformational space. After the annealing and equilibration steps, the periodic box was deformed along one axis to simulate a uniaxial tensile test, again in an NPT ensemble, with a constant strain rate while permitting fluctuations in cross-sectional area and pressure along the axes orthogonal to the deforming axis. Resulting pressure over the cross-section was computed at each time step to obtain the stress-strain curves in Figure 2. The setup and simulation process, which is outlined in more detail in the following sections, was repeated from start to finish 5 times for each system in Table 1, beginning with different initial conformations to observe the stochasticity of equilibrium density and mechanical response.

4.1. Model Assumptions and Sequences Studied. The model proteins are based on foot protein type 5 of the Mediterranean mussel Mytilus galloprovincialis, the structure of which can be accessed with UniProt ID Q6QZR3. fp5 is a 76-residue long nonrepetitive protein that differs by just two insertions and a single mutation from the 74residue ortholog in Mytilus edulis, the blue mussel.44 The rate of Y conversion to DOPA in both species is close to 100% resulting in a very high DOPA content of 28 mol %<sup>45</sup> with S also being variably modified to phosphoserine. The frequency of neighbor pairs of basic amino acids and DOPA residues has been closely scrutinized as a contributor to underwater adhesion of fp5 orthologs across species with a focus on the more abundant K over R and histidine (H).  $^{46-48}$  K and R, having side chain acid dissociation constants of 10.53 and 12.48, respectively, readily accept protons on their side chains over a wider range of physiologically relevant pH compared to H, which has a dissociation constant of 6.0. Interestingly, there are still five instances of neighboring DOPA and H pairs in fp5 and no occurrences of R adjacent to DOPA from which one could propose some interchangeability between K and H. That being said, due to their comparatively high pK values, R and K were modeled with protonated side chains in this study, while H was modeled with a net neutral charge assuming that they are all exposed to similar conditions. Although the DOPA content is evenly distributed throughout the protein, 81.25% of K is found in the 38 residues closest to the C-terminus of the protein. Based on the circulating theoretical mechanisms of cohesion, namely, cation  $-\pi$  interactions,  $\pi$  – $\pi$  stacking, and ionic cross-linking, the uneven distribution of the residues that primarily contribute to these interactions suggested that the two halves of the proteins would exhibit very different cohesive behavior. This possibility was examined by splitting the protein in half and simulating each of the resulting 38-residue long chains independently. To focus this work on interactions between basic and aromatic residues, Y residues were not modified to DOPA to match the one hydroxyl group

present in S and S residues were not modified to phosphoserine. Protein melts were modeled without covalent cross-linking of any kind. For the described mutations, it should be noted that covalent dityrosine crosslinks have significant impact on deformation mechanisms of the mussel plaque. The results of a study on the effects of dityrosine cross-linking density on the mechanical properties reported in this work are presented in Figure S5. We show that dityrosine conversion of up to 50% does not induce strain hardening up to 40% strain, the upper limit over which plateau stress is defined in this study, nor does it significantly impact the elastic modulus and toughness. Additionally, the assumption of 10% water content ensures that the melt will behave like a solid but likely does not reflect the water content of the adhesive protein in underwater conditions. For this reason, the water content was enhanced to 30% and then 50% to identify a limit of water content beyond which the results reported in this study are no longer relevant. Figure S6 shows that the effect of mutations is mostly preserved at 30% water content, but with much lower absolute toughness and plateau stress values. At 50% water, toughness and plateau stress are reduced to less than 5% of their original value, which is the point where cross-linking may be required to reclaim any solid-like properties. We also note that there are a number of other differences described above in the models selected for this study relative to real fp5s as they function in their biological milieu. These distinctions arise from the fact that our study is more geared toward guiding synthetic biology efforts to link primary protein sequence to mechanical properties. The distinctions and assumptions made are the following: (1) molecular weight of split proteins is approximately half of natural proteins, (2) no S residues were mutated to phosphoserine, (3) there were no covalent cross-links of any kind, (4) no high coordination  $(Fe^{3+})$  type metal ions were incorporated, but chloride counterions were added in varying fraction to balance charge, (5) overall water content was approximated at 10% by weight, (6) K and R were the only residues modeled in a protonated state other than terminal residues, and (7) Y was not modified to DOPA as this modification detrimentally impacts  $\pi$ -cation interactions.<sup>2</sup>

**4.2. Molecular Dynamics Simulations.** The initial configuration of fp5 peptides was generated using the PeptideBuilder Python library for generating peptide models with prespecified backbone angles. 49 To prevent the peptides from overlapping with themselves in the initial configuration, initial backbone angles were generated randomly and restricted between 120 and 240° such that the chains started out in an extended conformation. For each simulation, 24 individual peptides were generated in the Protein Data Bank (PDB) format using this procedure. For the melt systems with two different chain types, 12 chains of each type were generated. The number of water molecules necessary to achieve a protein to water mass ratio of 9:1 was calculated, as was the number of chloride ions required to neutralize the system's net charge. Packmol, which is a program that can pack a number of initial structures into a simulation box of predetermined size, was used to combine the protein, water, and chloride PDB files into a single simulation box without atomic overlap to avoid large repulsive van der Waals forces at the beginning of the simulation. The output PDB structure from Packmol was split by segment ID so that water molecules, chloride ions, and each individual protein chain were stored in separate PDB files for compatibility with the Visual Molecular Dynamics (VMD) psfgen Plugin, version 1.6.4.51 The protein structure file (PSF) was constructed using the CHARMM36 force field with the dihedral correction map (cmap) for proteins and ions<sup>52</sup> and TIP3 for water molecules. 53-55 The force field files were accessed via the homepage of the MacKerell Lab at the University of Maryland School of Pharmacy. In VMD version 1.9.3, the CHARMM topology and parameter files were first read by using the topology command. Histidine residues were modeled in their neutral state by aliasing the residue type from HIS to HSE in VMD. The individual PDBs for each chain were loaded into VMD as separate segments following the procedure outlined in the psfgen User's Guide, at which point a PSF file was written out using the writepsf command. Once a PSF file was generated by applying the CHARMM force field, the charmm2lammps.pl script developed at Sandia National Laboratories was used to translate the PDB, PSF, topology, parameter, and cmap files into the LAMMPS data file format.

4.2.1. Equilibrium Simulations and Density Analysis. All-atom MD simulations were performed in LAMMPS using real units, fully periodic boundary conditions, and a 1 fs time step. The angle and dihedral styles were set to charmm, and the bond and improper styles were set to harmonic for compatibility with the CHARMM force field parameters. Pairwise nonbonded interactions were computed using the lj/charmm/ coul/long pair style with inner and outer cutoff distances of 8 and 12 Å. To compute the Lennard-Jones potential between atoms, arithmetic mixing rules were applied to the nonbonded coefficients,  $\sigma$  and  $\epsilon$ . The special bonds charmm command was used to set weighting factors to scale the pairwise potential between bonded atoms. Long range potentials were computed using a standard Ewald summation with an accuracy of  $1 \times 10^{-6}$  using the kspace style command. Bond and angle constraints were applied to water molecules using the SHAKE algorithm during both equilibrium and nonequilibrium MD.<sup>56</sup> The system started off at a density of approximately 0.05 kg/m<sup>3</sup>, so that all of the extended chains could be accommodated by a single simulation box without overlap. To bring the system to its conformation immediately before the uniaxial deformation tests, a series of temperature and pressure annealing steps were performed in an NPT ensemble before a final NPT equilibration step at constant temperature and pressure to measure the system's density. The default Nosé-Hoover thermostat and barostat applied by the fix npt command were used to moderate temperature and pressure fluctuations with relaxation times of 100 and 1000 time steps, respectively. Chain mobility was very low over nanosecond time scales, so a series of annealing steps were performed to sample a larger conformation space over a shorter period of time. After annealing, temperature and pressure were held constant at 300 K and 1 atm over 5 ns, at which point the density of each system was recorded. During the annealing process, temperature and pressure were ramped and relaxed one variable at a time between 300 and 1000 K and 1 and 1000 atm. Annealing steps were run in the following order: temperature and pressure were held constant at 300 K and 1 atm for 2 ns, pressure was ramped from 1 to 1000 atm over 0.5 ns, temperature was ramped from 300 to 1000 K over 0.5 ns, temperature and pressure were held constant at 1000 K and 1000 atm for 1 ns, temperature was relaxed from 1000 to 300 K over 1 ns, pressure was relaxed from 1000 to 1 atm over 1 ns, and temperature and pressure were again held constant at 300 K and 1 atm over 5 ns. To confirm that the melts were responsive to the chosen annealing protocol, evolution of the radius of gyration  $(R_g)$  was tracked throughout the equilibrium procedure. Figure S9 demonstrates that fluctuations in  $R_{\rm g}$  were induced by temperature and pressure annealing and were stabilized upon "quenching". It should be noted that quantities derived from molecular dynamics simulations cannot provide certainty that the global energy minimum has been reached, but chain metrics like  $R_g$  can be used to predict how quickly the disordered phase of the free energy landscape is being sampled.<sup>57</sup> Equilibrium density, as reported in Figure 1d, was measured by taking the average density over the final 1 ns. Residue contacts counted in Figure S4 were identified by analyzing MD trajectories using the Python library MDA palysis 58,59 MDAnalysis.

4.2.2. Cohesive Energy Density Calculation. Cohesive energy density for the entire protein melt, water, and ion systems were calculated by definition of the heat of vaporization, which measures the energy required to transform the condensed phase into a collection of isolated components:<sup>60</sup>

$$E_{\rm coh} = \sum_{i=1}^{n} U_i - U_{\rm condense} \tag{1}$$

Here, n is the number of individual component molecules and ions;  $U_i$  is the potential energy of the isolated component representing intramolecular potential energy; and  $U_{\rm condense}$  represents the simulation's average potential energy in the condensed phase. Since the initial density of melts was less than 5% of the equilibrium condition, this state was assumed as a phase of isolated chains where intermolecular forces were negligible compared to the condensed phase. The cohesive energy could then be calculated as the difference between potential energy of the initial and final conformations of

equilibrium simulations. Cohesive energy density (CED) was then calculated by dividing the resulting value by the molar volume  $(V_m)$ .

$$CED = \frac{E_{\text{coh}}}{V_{\text{m}}} \tag{2}$$

4.2.3. Uniaxial Deformation Simulations and Analysis. Immediately after the final 5 ns equilibration step, uniaxial deformation tests were performed using the fix deform command in LAMMPS. An engineering strain rate of 108 per second was exerted over 20 ns to extend the initial box to a maximum strain of 200%. Such a high strain rate is necessary to perform mechanical tests on so many sequences at practicable computational expense. However, at strain rates of this magnitude, polymeric materials exhibit glassy behavior that manifests as an unrealistically high stress response. In these cases, we operate under the uncertain assumption that the impact of changing chemistry on stress response is independent of strain rate. We demonstrate in Figure S7 that this assumption holds for a subset of our simulations over a 1 order of magnitude decrease in strain rate to 10<sup>7</sup> per second, which is the longest simulation that could be realistically conducted for so many protein sequences. According to Figure S7a,b, the melts exhibit the expected behavior of stress response directly correlating with strain rate characteristic of polymeric materials, while Figure S7c,d demonstrates that impact of mutation on properties holds over this range of strain rates. Stress was measured in the plane normal to the pulling direction and fluctuated around 0 in the planes parallel to the deformation. During the deformation, components of the stress tensor orthogonal to the pulling direction were barostatted to 0 atm, so that the resulting stress on the simulation box was isolated to the plane normal to the pulling axis. Since fluctuations of stress are very large during MD tensile tests, a moving time average was applied using a centered window of size of 100 ps to obtain the stress-strain curves shown in Figure 2. The stress values from this moving average were also used to estimate the toughness, elastic modulus, and plateau stress reported in Figure 3. Toughness was calculated by numerically integrating the stress over strain from 0.01 to 0.40, elastic modulus was calculated as the linear slope between 0.01 and 0.03 strain, and the plateau stress was approximated as the average stress measured between 0.20 and 0.40 strain.

#### ASSOCIATED CONTENT

#### **Data Availability Statement**

Code and instructions to generate and run the simulations at 10% water content are available for download at https://github.com/keten-group/Split\_Mfp5\_Simulations.

#### Supporting Information

The Supporting Information is available free of charge at https://pubs.acs.org/doi/10.1021/acsbiomaterials.3c00088.

Analysis of the average strain at void onset across five MD runs and analysis of center of mass residues contacts distinguishing like and unlike chain contacts, density and mechanical property calculations for a the studied systems conducted in a controlled volume environment (NVT ensemble), analysis of mechanical properties of dityrosine cross-linked systems, systems with 30% and 50% water content, radial distribution functions of chloride surrounding certain protein residues, a summary of radius of gyration, and mechanical tests with strain rate decreased by 1 order of magnitude (PDF)

#### AUTHOR INFORMATION

#### **Corresponding Author**

Sinan Keten — Northwestern University, Department of Mechanical Engineering, Evanston, Illinois 60208, United States; Northwestern University, Department of Civil and Environmental Engineering, Evanston, Illinois 60208, United States; o orcid.org/0000-0003-2203-1425; Email: s-keten@northwestern.edu

#### Author

Jacob J. Graham – Northwestern University, Department of Mechanical Engineering, Evanston, Illinois 60208, United States

Complete contact information is available at: https://pubs.acs.org/10.1021/acsbiomaterials.3c00088

#### Notes

The authors declare no competing financial interest.

#### ACKNOWLEDGMENTS

S.K. acknowledges support from the National Science Foundation (Grant No. 2219149). J.G. was supported by the NSF Graduate Research Fellowship (Grant No. DGE-1842165) and the Ryan Fellowship organized through the International Institute for Nanotechnology at Northwestern University. This research was supported in part through the computational resources and staff contributions provided for the Quest high performance computing facility at Northwestern University which is jointly supported by the Office of the Provost, the Office for Research, and Northwestern University Information Technology.

#### REFERENCES

- (1) Tamarin, A.; Lewis, P.; Askey, J. The structure and formation of the byssus attachment plaque in Mytilus. *Journal of Morphology* **1976**, 149, 199–221.
- (2) Benedict, C. V.; Waite, J. H. Location and analysis of byssal structural proteins of Mytilus edulis. *Journal of Morphology* **1986**, *189*, 171–181
- (3) Smyth, J. D. A Technique for the Histochemical Demonstration of Polyphenol Oxidase and its application to Egg-shell Formation in Helminths and Byssus Formation in Mytilus. *Journal of Cell Science* **1954**, s3–95, 139–152.
- (4) Qin, Z.; Buehler, M. J. Impact tolerance in mussel thread networks by heterogeneous material distribution. *Nat. Commun.* **2013**, *4*, 2187.
- (5) Filpula, D. R.; Lee, S. M.; Link, R. P.; Strausberg, S. L.; Strausberg, R. L. Structural and Functional Repetition in a Marine Mussel Adhesive Protein. *Biotechnol. Prog.* **1990**, *6*, 171–177.
- (6) Waite, J. H.; Housley, T. J.; Tanzer, M. L. Peptide Repeats in a Mussel Glue Protein: Theme and Variations. *Biochemistry* **1985**, *24*, 5010–5014.
- (7) Brown, C. H. Some Structural Proteins of Mytilus edulis. Quarterly Journal of Microscopical Science 1952, s3–93, 487–502.
- (8) Zhao, H.; Waite, J. H. Linking adhesive and structural proteins in the attachment plaque of Mytilus californianus. *J. Biol. Chem.* **2006**, 281, 26150–26158.
- (9) Papov, V. V.; Diamond, T. V.; Biemann, K.; Waite, J. H. Hydroxyarginine-containing polyphenolic proteins in the adhesive plaques of the marine mussel Mytilus edulis. *J. Biol. Chem.* **1995**, 270, 20183–20192.
- (10) DeMartini, D. G.; Errico, J. M.; Sjoestroem, S.; Fenster, A.; Waite, J. H. A cohort of new adhesive proteins identified from transcriptomic analysis of mussel foot glands. *J. R. Soc., Interface* **2017**, *14*, 20170151.
- (11) Rzepecki, L. M.; Hansen, K. M.; Waite, J. H. Characterization of a Cystine-Rich Polyphenolic Protein Family from the Blue Mussel Mytilus edulis L. *Biological Bulletin* **1992**, *183*, 123–137.
- (12) Waite, J. H.; Harrington, M. J. Following the thread: Mytilus mussel byssus as an inspired multi-functional biomaterial. *J. Comput. Chem.* **2022**, *100*, 197–211.
- (13) Valois, E.; Mirshafian, R.; Waite, J. H. Phase-dependent redox insulation in mussel adhesion. *Science Advances* **2020**, *6*, No. eaaz6486.

- (14) Waite, J. H.; Qin, X. X.; Coyne, K. J. The peculiar collagens of mussel byssus. *Matrix Biology* **1998**, *17*, 93–106.
- (15) Taylor, S. W.; Chase, D. B.; Emptage, M. H.; Nelson, M. J.; Waite, J. H. Ferric Ion Complexes of a DOPA-Containing Adhesive Protein from Mytilus edulis. *Inorg. Chem.* **1996**, *35*, 7572–7577.
- (16) Hwang, D. S.; Zeng, H.; Masic, A.; Harrington, M. J.; Israelachvili, J. N.; Waite, J. H. Protein- and metal-dependent interactions of a prominent protein in mussel adhesive plaques. *J. Biol. Chem.* **2010**, 285, 25850–25858.
- (17) Harrington, M. J.; Masic, A.; Holten-Andersen, N.; Waite, J. H.; Fratzl, P. Iron-Clad Fibers: A Metal-Based Biological Strategy for Hard Flexible Coatings. *Science* **2010**, 328, 216–220.
- (18) Zeng, H.; Hwang, D. S.; Israelachvili, J. N.; Waite, J. H. Strong reversible Fe<sup>3+</sup>-mediated bridging between dopa-containing protein films in water. *Proc. Natl. Acad. Sci. U.S.A.* **2010**, *107*, 12850–12853.
- (19) Schmitt, C. N.; Winter, A.; Bertinetti, L.; Masic, A.; Strauch, P.; Harrington, M. J. Mechanical homeostasis of a DOPA-enriched biological coating from mussels in response to metal variation. *J. R. Soc., Interface* **2015**, *12*, 20150466.
- (20) Kim, E.; Dai, B.; Qiao, J. B.; Li, W.; Fortner, J. D.; Zhang, F. Microbially Synthesized Repeats of Mussel Foot Protein Display Enhanced Underwater Adhesion. *ACS Appl. Mater. Interfaces* **2018**, *10*, 43003–43012.
- (21) Gebbie, M. A.; Wei, W.; Schrader, A. M.; Cristiani, T. R.; Dobbs, H. A.; Idso, M.; Chmelka, B. F.; Waite, J. H.; Israelachvili, J. N. Tuning underwater adhesion with cation- $\pi$  interactions. *Nat. Chem.* **2017**, *9*, 473–479.
- (22) Perrini, M.; Barrett, D.; Ochsenbein-Koelble, N.; Zimmermann, R.; Messersmith, P.; Ehrbar, M. A comparative investigation of musselmimetic sealants for fetal membrane repair. *Journal of the Mechanical Behavior of Biomedical Materials* **2016**, *58*, 57–64.
- (23) Balkenende, D. W.; Winkler, S. M.; Messersmith, P. B. Marine-inspired polymers in medical adhesion. *Eur. Polym. J.* **2019**, *116*, 134–143
- (24) North, M. A.; Del Grosso, C. A.; Wilker, J. J. High Strength Underwater Bonding with Polymer Mimics of Mussel Adhesive Proteins. *ACS Appl. Mater. Interfaces* **2017**, *9*, 7866–7872.
- (25) Dunbar, M.; Keten, S. Energy Renormalization for Coarse-Graining a Biomimetic Copolymer, Poly(catechol-styrene). *Macromolecules* **2020**, *53*, 9397–9405.
- (26) Cheng, B.; Yu, J.; Arisawa, T.; Hayashi, K.; Richardson, J. J.; Shibuta, Y.; Ejima, H. Ultrastrong underwater adhesion on diverse substrates using non-canonical phenolic groups. *Nat. Commun.* **2022**, 13, 1892.
- (27) Lee, B. P.; Messersmith, P. B.; Israelachvili, J. N.; Waite, J. H. Mussel-inspired adhesives and coatings. *Annu. Rev. Mater. Res.* **2011**, 41. 99–132.
- (28) Kim, E.; Jeon, J.; Zhu, Y.; Hoppe, E. D.; Jun, Y. S.; Genin, G. M.; Zhang, F. A Biosynthetic Hybrid Spidroin-Amyloid-Mussel Foot Protein for Underwater Adhesion on Diverse Surfaces. *ACS Appl. Mater. Interfaces* **2021**, *13*, 48457–48468.
- (29) Li, J.; Jiang, B.; Chang, X.; Yu, H.; Han, Y.; Zhang, F. Bi-terminal fusion of intrinsically-disordered mussel foot protein fragments boosts mechanical strength for protein fibers. *Nat. Commun.* **2023**, *14*, 2127.
- (30) Li, Y.; Cheng, J.; Delparastan, P.; Wang, H.; Sigg, S. J.; DeFrates, K. G.; Cao, Y.; Messersmith, P. B. Molecular design principles of Lysine-DOPA wet adhesion. *Nat. Commun.* **2020**, *11*, 3895.
- (31) Petrone, L.; Kumar, A.; Sutanto, C. N.; Patil, N. J.; Kannan, S.; Palaniappan, A.; Amini, S.; Zappone, B.; Verma, C.; Miserez, A. Mussel adhesion is dictated by time-regulated secretion and molecular conformation of mussel adhesive proteins. *Nat. Commun.* **2015**, *6*, 8737
- (32) Desmond, K. W.; Zacchia, N. A.; Waite, J. H.; Valentine, M. T. Dynamics of mussel plaque detachment. *Soft Matter* **2015**, *11*, 6832–6839.
- (33) Waite, J. H. Results and problems in cell differentiation 1992, 19, 27–54.
- (34) Packer, M. S.; Liu, D. R. Methods for the directed evolution of proteins. *Nat. Rev. Genet.* **2015**, *16*, 379–394.

- (35) Yang, K. K.; Wu, Z.; Arnold, F. H. Machine-learning-guided directed evolution for protein engineering. *Nat. Methods* **2019**, *16*, 687–694
- (36) Yu, C. H.; Khare, E.; Narayan, O. P.; Parker, R.; Kaplan, D. L.; Buehler, M. J. ColGen: An end-to-end deep learning model to predict thermal stability of *de novo* collagen sequences. *Journal of the Mechanical Behavior of Biomedical Materials* **2022**, 125, 104921.
- (37) Zhu, J.; Jia, Y.; Lei, J.; Liu, Z. Deep learning approach to mechanical property prediction of single-network hydrogel. *Mathematics* **2021**, *9*, 2804.
- (38) Arakawa, K.; et al. 1000 spider silkomes: Linking sequences to silk physical properties. *Science advances* **2022**, 8, No. eabo6043.
- (39) Fu, L.; Li, H. Toward Quantitative Prediction of the Mechanical Properties of Tandem Modular Elastomeric Protein-Based Hydrogels. *Macromolecules* **2020**, *53*, 4704–4710.
- (40) Vollrath, F.; Porter, D. Spider silk as a model biomaterial. *Applied Physics A: Materials Science and Processing* **2006**, 82, 205–212.
- (41) Chen, A. B.; Shao, Q.; Hall, C. K. Molecular simulation study of 3, 4-dihydroxyphenylalanine in the context of underwater adhesive design. *J. Chem. Phys.* **2021**, *154*, 144702.
- (42) Khani, M.; Materzok, T.; Eslami, H.; Gorb, S.; Müller-Plathe, F. Water uptake by gecko  $\beta$ -keratin and the influence of relative humidity on its mechanical and volumetric properties. *J. R. Soc., Interface* **2022**, 19, 20220372.
- (43) Thompson, A. P.; Aktulga, H. M.; Berger, R.; Bolintineanu, D. S.; Brown, W. M.; Crozier, P. S.; in 't Veld, P. J.; Kohlmeyer, A.; Moore, S. G.; Nguyen, T. D.; Shan, R.; Stevens, M. J.; Tranchida, J.; Trott, C.; Plimpton, S. J. LAMMPS a flexible simulation tool for particle-based materials modeling at the atomic, meso, and continuum scales. *Comput. Phys. Commun.* **2022**, *271*, 108171.
- (44) Hwang, D. S.; Yoo, H. J.; Jun, J. H.; Moon, W. K.; Cha, H. J. Expression of functional recombinant mussel adhesive protein Mgfp-5 in *Escherichia coli. Appl. Environ. Microbiol.* **2004**, *70*, 3352–3359.
- (45) Waite, J. H.; Qin, X. Polyphosphoprotein from the adhesive pads of Mytilus edulis. *Biochemistry* **2001**, *40*, 2887–2893.
- (46) Ou, X.; Xue, B.; Lao, Y.; Wutthinitikornkit, Y.; Tian, R.; Zou, A.; Yang, L.; Wang, W.; Cao, Y.; Li, J. Structure and sequence features of mussel adhesive protein lead to its salt-tolerant adhesion ability. *Science Advances* **2020**, *6*, No. eabb7620.
- (47) Qin, Z.; Buehler, M. J. Molecular mechanics of mussel adhesion proteins. *Journal of the Mechanics and Physics of Solids* **2014**, 62, 19–30.
- (48) Maier, G. P.; Rapp, M. V.; Waite, J. H.; Israelachvili, J. N.; Butler, A. Adaptive synergy between catechol and lysine promotes wet adhesion by surface salt displacement. *Science* **2015**, 349, 628–632.
- (49) Tien, M. Z.; Sydykova, D. K.; Meyer, A. G.; Wilke, C. O. Peptidebuilder: A simple python library to generate model peptides. *PeerJ.* **2013**, *1*, No. e80.
- (50) Martínez, L.; Andrade, R.; Birgin, E. G.; Martínez, J. M. PACKMOL: A package for building initial configurations for molecular dynamics simulations. *J. Comput. Chem.* **2009**, *30*, 2157–2164.
- (51) Humphrey, W.; Dalke, A.; Schulten, K. VMD: Visual Molecular Dynamics. *J. Mol. Graphics* **1996**, *14*, 33–38.
- (52) Huang, J.; Rauscher, S.; Nawrocki, G.; Ran, T.; Feig, M.; De Groot, B. L.; Grubmüller, H.; MacKerell, A. D. CHARMM36m: An improved force field for folded and intrinsically disordered proteins. *Nat. Methods* **2017**, *14*, 71–73.
- (53) Jorgensen, W. L.; Chandrasekhar, J.; Madura, J. D.; Impey, R. W.; Klein, M. L. Comparison of simple potential functions for simulating liquid water. *J. Chem. Phys.* **1983**, *79*, 926–935.
- (54) Price, D. J.; Brooks, C. L. A modified TIP3P water potential for simulation with Ewald summation. *J. Chem. Phys.* **2004**, *121*, 10096–10103.
- (55) MacKerell, A. D.; et al. All-atom empirical potential for molecular modeling and dynamics studies of proteins. *J. Phys. Chem. B* **1998**, *102*, 3586–3616.
- (56) Ryckaert, J. P.; Ciccotti, G.; Berendsen, H. J. Numerical integration of the cartesian equations of motion of a system with constraints: molecular dynamics of *n*-alkanes. *J. Comput. Phys.* **1977**, 23, 327–341.

- (57) Gartner, T. E.; Jayaraman, A. Modeling and Simulations of Polymers: A Roadmap. *Macromolecules* **2019**, *52*, 755–786.
- (58) Gowers, R.; Linke, M.; Barnoud, J.; Reddy, T.; Melo, M.; Seyler, S.; Domański, J.; Dotson, D.; Buchoux, S.; Kenney, I.; Beckstein, O. MDAnalysis: A Python Package for the Rapid Analysis of Molecular Dynamics Simulations. *Proceedings of the 15th Python in Science Conference*; SciPy: 2016, pp 98–105.
- (59) Michaud-Agrawal, N.; Denning, E. J.; Woolf, T. B.; Beckstein, O. Software News and Updates MDAnalysis: A Toolkit for the Analysis of Molecular Dynamics Simulations. *J. Comput. Chem.* **2011**, *32*, 2319–2327.
- (60) Li, C.; Strachan, A. Cohesive energy density and solubility parameter evolution during the curing of thermoset. *Polymer* **2018**, *135*, 162–170.

### **□** Recommended by ACS

## Toward Protein-Repellent Surface Coatings from Catechol-Containing Cationic Poly(2-ethyl-2-oxazoline)

Nils Lüdecke, Helmut Schlaad, et al.

APRIL 06, 2023

ACS APPLIED MATERIALS & INTERFACES

READ 🗹

#### Ternary Synergy of Lys, Dopa, and Phe Results in Strong Cohesion of Peptide Films

Heng Chang, Xavier Banquy, et al.

JANUARY 09, 2023

ACS APPLIED BIO MATERIALS

READ 🗹

#### Mussels Fabricate Porous Glues via Multiphase Liquid-Liquid Phase Separation of Multiprotein Condensates

Max Renner-Rao, Matthew J. Harrington, et al.

NOVEMBER 22, 2022

ACS NANO

READ 🗹

#### Tyrosine's Unique Role in the Hierarchical Assembly of Recombinant Spider Silk Proteins: From Spinning Dope to Fibers

Dillan Stengel, Gregory P. Holland, et al.

FEBRUARY 15, 2023

BIOMACROMOLECULES

READ 🗹

Get More Suggestions >